



## UvA-DARE (Digital Academic Repository)

### Fluorescent molecular rotors

*From working principles to visualization of mechanical contacts*

Suhina, T.

#### Publication date

2017

#### Document Version

Other version

#### License

Other

[Link to publication](#)

#### Citation for published version (APA):

Suhina, T. (2017). *Fluorescent molecular rotors: From working principles to visualization of mechanical contacts*. [Thesis, fully internal, Universiteit van Amsterdam].

#### General rights

It is not permitted to download or to forward/distribute the text or part of it without the consent of the author(s) and/or copyright holder(s), other than for strictly personal, individual use, unless the work is under an open content license (like Creative Commons).

#### Disclaimer/Complaints regulations

If you believe that digital publication of certain material infringes any of your rights or (privacy) interests, please let the Library know, stating your reasons. In case of a legitimate complaint, the Library will make the material inaccessible and/or remove it from the website. Please Ask the Library: <https://uba.uva.nl/en/contact>, or a letter to: Library of the University of Amsterdam, Secretariat, Singel 425, 1012 WP Amsterdam, The Netherlands. You will be contacted as soon as possible.

## Molecular Rotors for Contact Area Visualization\*

### Abstract

In this work we characterize and compare three molecular rotors immobilized on a glass surface for the purpose of imaging the microscopic contact area between surfaces with molecular sensitivity and high spatial resolution. Because the signal that discriminates contacts from background originates from molecular emitters, such method offers a considerable improvement in axial contact discrimination over optical measurements based on interference patterns of the reflected light. While the fluorescence of the two examined molecular rotors based on the dicyanomethylenedihydrofuran (DCDHF) accepting unit is significantly enhanced within the contact zone, the molecular rotor based on unhindered *meso*-substituted boron-dipyrromethane unexpectedly does not show confinement-induced response. Uniformly distributed fluorescence lifetimes of DCDHF molecular rotors confined between a glass cover slips and a polystyrene bead point towards the presence of unresolved asperities that are homogeneously distributed throughout the contact between the examined objects. Comparison of spectra and fluorescence lifetimes of DCDHF rotors in solution and in contacts shows that the confinement in the contact areas is homogeneous, but not complete. The environment is more like a viscous liquid.

---

\* This chapter is adapted from:  
Suhina, T; Weber, B.; Petrova, D.; Bonn, D.; Brouwer, A. M., *in preparation*.

We have recently reported a contact imaging method (see Scheme 7.1) which makes use of the fluorescence response of viscosity-sensitive molecular rotors based on the dicyanomethylenedihydrofuran (DCDHF) acceptor unit (compound **1** in Scheme 7.1).<sup>1</sup> We developed this method<sup>1</sup> in order to contribute towards understanding the relation between contacts and friction, which is considered to be responsible for for approximately one third of the world energy consumption.<sup>2</sup> Frictional force is commonly quantified by  $\vec{F} = \mu \vec{L}$ <sup>3,4</sup>, the expression which is nowadays referred to as Amontons' first law of friction and is known to be valid for a vast majority of frictional interfaces. In this expression, the magnitude of the frictional force ( $\vec{F}$ ) is directly proportional to the applied load ( $\vec{L}$ ) scaled by  $\mu$ , which is an experimentally determined and system-specific constant known as the friction coefficient.<sup>5</sup>

Real (microscopic) contact area and its relation to the friction coefficient  $\mu$  is, however, considered to be a crucial question towards understanding of friction mechanics.<sup>6,7</sup> Real surfaces are microscopically rough, and as a result of roughness, the real contact area differs from the macroscopic contact area. The relationship between the real area of contact and friction has been a subject of considerable theoretical work,<sup>8-13</sup> and many experimental attempts at measuring the real contact area have been made.<sup>8,14-19</sup> Contact area measurements were, however, either indirect or applicable for a very limited number of systems/object geometries and did not show sensitivity on a molecular scale. This rendered experimental confirmation of contact theories rather difficult, and the physical meaning of the friction coefficient is still not well understood.<sup>6,7</sup>

Our previously reported fluorescence microscopy contact imaging method<sup>1</sup> is based on enhanced fluorescence of molecular rotors under contact-induced confinement. Dye **1** is ideally suited for microscopy applications because it works well with the common excitation wavelength of 488 nm, for which optimized filter sets are available. We were interested in exploring the scope of this type of dye, in particular to allow excitation at longer wavelengths. Many red-shifted DCDHF dyes, however, are moderately to strongly fluorescent in non-viscous solvents.<sup>20</sup> These compounds are therefore not suitable for applications as probes of viscosity or confinement. The only exception among the published DCDHF dyes was the chromophore of compound **2** (Scheme 7.1),<sup>21,22</sup> which is conceptually derived from **1** by insertion of a C=C double bond between the aniline and DCDHF units. As we will show below, fluorophore **2** is similarly effective for probing confinement as **1**, but it is suitable for use with 532 nm excitation, another popular wavelength in microscopy and can be excited up to 600 nm.

BODIPY molecular rotors are well known as molecular probes of viscosity, and we considered them as an alternative means of probing confinement. Therefore we included compound **3** in the present study. In their excited state, DCDHF- and BODIPY-based molecular rotors perform geometrical distortions which result in efficient excited-state deactivation (fluorescence quenching).<sup>23,24</sup> Because such motions have significant spatial requirements, increasing the viscosity/rigidity of the molecular surroundings results in enhanced fluorescence from these molecules. In case of **1** and **2**, the same effect can be achieved locally when a surface with

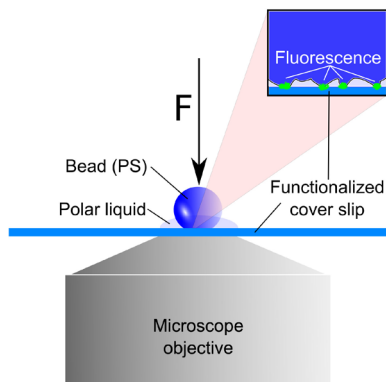


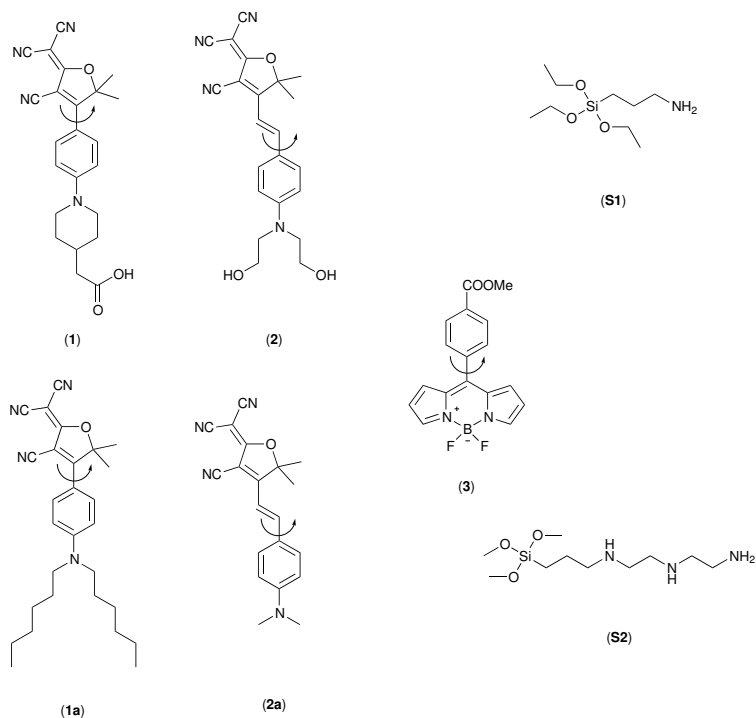
**Figure 7.1:** Schematic illustration of the setup used for contact imaging.

covalently attached molecular rotors is brought into contact with another surface. Molecular confinement takes place only where the two surfaces form a direct contact, and this enables contact visualization by means of fluorescence microscopy which provides excellent sensitivity and good spatial resolution.<sup>1</sup>

One question that was not addressed in our previous study is the nature and extent of confinement in a contact that gives rise to the fluorescence turn-on effect. Is the nonradiative decay of the probe molecules fully suppressed, or is there still some freedom of motion? Is there a variation in the degree of confinement within the contact area? Compounds used in the previous study (compounds **1** and **1a**) and current work (compounds **2**, **2a** and **3**), together with the silane linkers that were used to immobilize molecular rotors onto glass substrates (**S1** and **S2**) are shown in Scheme 7.2. While the fluorescence of molecular rotors **1** and **2** becomes significantly enhanced upon confinement, the fluorescence quantum yield of compound **3** based on *meso*-substituted boron-dipyrromethane (BODIPY) does not change, despite the fact that it shows pronounced viscosity response in liquids.

The work presented in this paper is divided into three parts. In the first part, we characterize and compare the behavior of the three examined molecular rotors and relate the changes in their fluorescence response to the changes in viscosity of their local environment. In the second part, we examine the photophysical properties of the molecular rotors covalently attached onto a glass substrate. For this purpose, we use **1** as a model system and examine the influence of two silane linkers (**S1** and **S2**) on the photophysical properties of the surface-attached probe. To study the effect of surface-bound chromophore concentration, we introduce the inert cyclohexane acetic acid (CHAA) as a "spacer" together with **1**. Measured fluorescence lifetimes and emission peak maxima allow us to estimate the polarity of the environment in which immobilized molecular rotors reside, and to assess whether self-quenching processes occur. In the final part, we demonstrate the applicability of **1** and **2** for contact area measurements by means of intensity and lifetime based fluorescence imaging methods, and discuss the benefits of our method over the reflection-based contact measurement. We additionally discuss the potential reasons behind the lack of response in contact imaging experiments

using BODIPY based probe **3**.



**Scheme 7.1:** Compounds used in this work. Arrows indicate bond rotations which lead to rapid nonradiative decay in polar solvents.

## 7.1 Experimental details

All solvents that were used in fluorescence measurements were of spectroscopic or HPLC grade. *N*1-(2-aminoethyl)-*N*2-(3-(trimethoxysilyl)propyl)ethane-1,2-diamine was purchased from Gelest. All other reagents were purchased from Sigma Aldrich. Experimental details for most experiments are explained in Chapter 2 of this thesis. Experimental details that are specific to this chapter are given below.

### Preparations of molecules

Preparation of compounds **1**,<sup>1</sup> **1a**,<sup>25</sup> and **3**<sup>26</sup> has been described elsewhere. Compound **2** was prepared by a procedure analogous to that for **2a**. All reactions were conducted under  $N_2$ .

**Compound 2a:** The preparation procedure was analogous to the one reported in ref. 22, but 4-dimethylaminobenzaldehyde was used instead of 4-diethylaminoben-

zaldehyde. 4-Dimethylaminobenzaldehyde (675 mg, 4.53 mmol) and 2-(3-cyano-4,5,5-trimethylfuran-2(5H)-ylidene)malononitrile (388 mg, 2.06 mmol) were dissolved in 18 mL of pyridine, and 3 drops of acetic acid were added. The mixture turned dark blue after approximately 10 minutes of stirring at room temperature. After 48 hours, the mixture was poured into 150 mL of ice-water and filtered. The precipitate was dissolved in  $\text{CH}_2\text{Cl}_2$ , washed thoroughly with water/brine and the organic solvent was evaporated. The obtained dark blue powder was reprecipitated from  $\text{CH}_2\text{Cl}_2/\text{MeOH}$  to give 211 mg of **2a** (31 %). A similar preparation of this compound can be found in ref. 27.  $^1\text{H}$  NMR (400 MHz,  $\text{CDCl}_3$ ):  $\delta$  (ppm) 1.76 (6H, s), 3.15 (6H, s), 6.70-6.78(3H, m), 7.53-7.63 (3H, m).  $^{13}\text{C}$  NMR (400 MHz,  $\text{CDCl}_3$ ):  $\delta$  (ppm) 26.79, 40.21, 53.42, 96.75, 108.84, 111.42, 111.85, 112.17, 112.63, 121.85, 132.18, 148.34, 153.75, 174.20, 176.23. CSI-MS: MH+ 331.38 (calculated), 331.15 (observed).

**Compound 2:** A mixture of 4-(bis(2-hydroxyethyl)amino)benzaldehyde (778 mg, 3.72 mmol) and 2-(3-cyano-4,5,5-trimethylfuran-2(5H)-ylidene)malononitrile (340 mg, 1.69 mmol) in pyridine (200 mL) was stirred at room temperature until all reagents dissolved. After that, 3 drops of acetic acid were added to this mixture, which turned dark after 10 minutes of stirring at room temperature. The reaction mixture was left to stir for 24 hours, after which it was poured into 150 mL of ice-water. 0.1 M HCl was added until a precipitate could be observed. This precipitate was filtered, and 140 mg of blue powder with a reddish shine was obtained (22 %). Preparation of this compound is also described in ref. 28.  $^1\text{H}$  NMR (400 MHz,  $\text{DMSO}-d_6$ ):  $\delta$  (ppm) 1.76 (6H, s), 3.61 (8H, s), 6.7-6.9 (3H, m), 7.6-8 (3H, m). CSI-MS: MH+ 391.44 (calculated), 391.18 (observed).

## Glass silanization

**Cleaning:** A rack with 4 borosilicate glass cover slips (2 cm  $\times$  2 cm  $\times$  170  $\mu\text{m}$ ) was sonicated in aqueous Extran solution (0.3 % w/w) for 30 mins, then sonicated in deionized water (10 min) and in ethanol (30 mins), dried under an air current, and placed in an ozone photoreactor for 2 hours.

**Silanization with 3-aminopropyltrimethoxysilane (APTES, S1):** 80 mL of aqueous ethanol (96 %, v/v) was mixed with a small amount of acetic acid (so that pH  $\sim$  5). To this mixture, APTES (**S1**, 2 mL) was added. Cover slips were placed in this solution and were left to react (with stirring) for 25-30 minutes. After this time, the cover slips were sonicated in ethanol 2 times for 30 minutes, dried in air, and annealed at 130  $^\circ\text{C}$  for 3 days.

**Silanization with N1-(2-aminoethyl)-N2-(3-(trimethoxysilyl)propyl)ethane-1,2-diamine (S2):** 80 mL of toluene was mixed with 0.2 mL of **S2**. Glass cover slips were immersed in this mixture and the reaction was left to proceed for 25 minutes (under nitrogen). Cover slips were afterwards sonicated in toluene and ethanol, dried under an air flow and annealed for 3 days at 130  $^\circ\text{C}$ .

### Immobilization of 1, 2 and 3

**CS1: 1** (15 mg, 0.037 mmol) was dissolved in 80 mg of dry dimethylformamide (DMF) under  $N_2$ . To this solution, (benzotriazol-1-yloxy)tris(dimethylamino)-phosphonium hexafluorophosphate (BOP; 100 mg, 0.230 mmol) and hydroxy-benzotriazole (HOBt; 35 mg, 0.23 mmol) were added. 120  $\mu$ L of N,N-diisopropyl-ethylamine (DIPEA) were added to this solution, and a rack with cover slips (previously functionalized with **S1**) was immersed in the solution. This was left to stir overnight. After that, cover slips were sonicated in ethanol twice for 15 minutes, and dried under an air current. Cover slips were stored in plastic containers until use.

**CS1-CHAA: 1** (15 mg, 0.037 mmol) and cyclohexane acetic acid (CHAA; 53 mg, 0.37 mmol) were dissolved in 80 mL of dry dimethylformamide (DMF) under  $N_2$ . To this solution, BOP (824 mg, 1.87 mmol) and HOBt (252 mg, 1.65 mmol) were added. 1.3 mL of N,N-diisopropylethylamine (DIPEA) were added, and a rack with cover slips (previously functionalized with **S1**) was immersed in the solution. This was left to stir overnight. After that, cover slips were sonicated in ethanol twice for 15 minutes, and dried under an air current. Cover slips were stored in plastic containers until use.

**CS1-L:** The samples were produced using the same quantities as **CS1**, only the cover slips functionalized with **S2** were used. Samples were stored in sealed plastic containers under Ar until use.

**CS2:** Compound **2** (10 mg, 0.025 mmol) was dissolved in dry dichloromethane under  $N_2$  atmosphere. To this solution, 15 % phosgene solution (0.50 mL, 0.66 mmol) in toluene was added. This solution was stirred for 5 minutes in order to provide enough time for the acylation reaction of phosgene with the alcohol groups to take place, after which a rack with silanized (**S1**) cover slips was added. This was stirred for approximately 20 minutes after which the cover slips were taken out and thoroughly washed in dichloromethane, toluene and ethanol by sonication for 15 minutes in each solvent. Samples were stored in sealed plastic containers under Ar until use.

**CS3:** BODIPY derivative **3** (10 mg, 0.031 mmol) was dissolved in 70 mL of dry DMF. Five drops of triethylamine were added, and a rack with cover slips was placed in the reaction flask. This mixture was heated to 50 °C and left to stir overnight. Cover slips were sonicated in ethanol (twice for 15 minutes), rinsed with dichloromethane, dried under an air current and stored in plastic containers under Ar until use.

### Polystyrene beads

550  $\mu$ m polystyrene spheres (microbeads) were purchased from the Precision Plastic Ball Company (Addingham, Ilkley, UK) and roughened by placing them over 240 grit sand paper on an orbital shaker (1200 rpm) for 2 days.

## Fluorescence microscopy and CCD spectra

**Fluorescence Lifetime Imaging:** Instrument description is given in Chapter 2. The spheres were pressed onto functionalised cover slips by applying an arbitrary external load, as our goal was not to examine contact area dependence on load with these experiments. Because of the nonexponential nature of the fluorescence decays, the difficulty in estimating of the instrument response function and short lifetime, the average fluorescence lifetimes reported for our FLIM data are defined as the average times that emitted photons take to reach the detector after the excitation pulse (fastFLIM).

**Cover Slip Emission Spectra:** Contact emission spectra could not be obtained using the SPEX Fluorolog, and were instead measured using the MicroTime 200 confocal microscope. Light captured by the objective was directed towards the attached spectrograph (Spectra Pro-150, Acton Research Instruments), and captured with a Princeton Instruments Photon Max 512 EM-CCD camera. Before measuring emission spectra within contact, the spectrograph was calibrated by measuring peaks of a Hg lamp and by comparing the fluorescence emission spectra of dry and wetted samples measured with SPEX Fluorolog and confocal microscope.

### CCD spectral fitting

In order to find consistent values of the fluorescence emission maxima measured with the EM-CCD camera, we fitted the raw measured spectra (in wavelength domain) with one or two exponentially convolved gaussian functions.<sup>29</sup>

### Steady state vis spectra

See Chapter 2 for details. Fluorescence quantum yields were measured relative to fluorescein in 0.1 M NaOH (**1a**, **3**;  $\Phi_f = 0.89$ <sup>30</sup>) or rhodamine 101 (**2a**;  $\Phi_f = 0.915$ <sup>30</sup>).

### Calculations

All Density Functional Theory (DFT) calculations were done with the Gaussian 09 software package (revision D.01).<sup>31</sup>

## 7.2 Results and discussion

### 7.2.1 Photophysical properties of molecular rotors in solution.

Because molecular rotors **1** and **2** possess polar functional groups (-COOH and -OH, respectively) that may cause specific interactions (such as hydrogen bonding) in solutions, compounds **1a** and **2a** were prepared as "clean" chromophore models

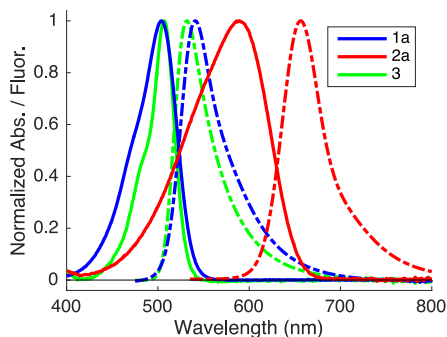
**Table 7.1:** Photophysical properties of the examined chromophores in solution and immobilized on glass cover slips.

Variable	1a	2a	3	CS1	CS1-L	CS1-CHAA	CS2
$\lambda_{\text{em,dry}}$ (nm)	-	-	-	521	526	521	634
$\lambda_{\text{em,toluene}}$ (nm)	509	605	530	-	-	-	-
$\lambda_{\text{em,DMSO}}$ (nm)	542	656	532	541	-	-	654
$\lambda_{\text{em,contact}}$ (nm)	-	-	-	535*	-	-	637*
$\tau_{\text{avg,dry}}$ <sup>a</sup> (ns)	-	-	-	1.5 (~1.3)	1.4	1.7 (~1.8)	(~1.7)
$\tau_{\text{avg,DMSO/MeCN}}$ <sup>b</sup> (ps)	27	77	50	<400	-	-	(~1000)
$\tau_{\text{avg,glycerol}}$ <sup>c</sup> (ns)	1.34	1.22	-	1.3	1.4	1.5	-
$\tau_{\text{avg,contact}}$ <sup>d</sup> (ns)	-	-	-	1.5	-	-	1.8
$\tau_{\text{avg,PMMA}}$ (ns)	2.7	2.4	7.3	-	-	-	-
$\Phi_{\text{f}}$ <sup>e</sup> (%)	0.5	1.4	0.5	-	-	-	-

<sup>a</sup> Values obtained by single photon counting (IRF FWHM  $\approx$  24 ps), decays fitted using triexponential function. Values in brackets obtained with TCSPC unit of a confocal microscope (FWHM  $\approx$  0.4 ns), average lifetimes estimated by fast FLIM procedure; <sup>b</sup> fluorescence lifetime of **3** measured in MeCN, others in DMSO; decay curves for **CS1** and **CS2** were measured with TCSPC unit of our confocal microscope; <sup>c</sup> slowest component of triexponential fit in solutions for **1a** and **2a** (negative amplitudes observed for other components at some wavelengths); <sup>d</sup> measured with TCSPC unit of a confocal microscope; <sup>e</sup> Fluorescence quantum yields for **1a**, **3** and **2a** obtained from ref. 24, Chapter 6, and measured relative to R101 in EtOH ( $\Phi_{\text{f}} = 0.915$ ),<sup>30</sup> respectively; \* from fits of the fluorescence spectra measured with EM-CCD camera on confocal microscope.

and used in experiments in which immobilization was not required. Electronic absorption and emission spectra in polar DMSO are shown in Figure 7.2. All three molecules absorb and fluoresce in the visible spectral range at relatively low energies, which makes them convenient chromophores for use in microscopy experiments. Molecular rotor **2** (**2a**) has an obvious advantage for microscopy applications, as its absorption and emission spectra are significantly red-shifted compared to chromophores **1** and **3**. In DMSO, all three compounds exhibit very low fluorescence quantum yields (0.5 %, 1.4 % and 0.5 % for **1a**, **2a** and **3**, respectively).

**1a**, **2a** and **3** exhibit very short fluorescence lifetimes in polar DMSO and

**Figure 7.2:** Normalized steady state electronic absorption (solid lines) and emission (dashed lines) spectra of **1a**, **2a** and **3** in DMSO.

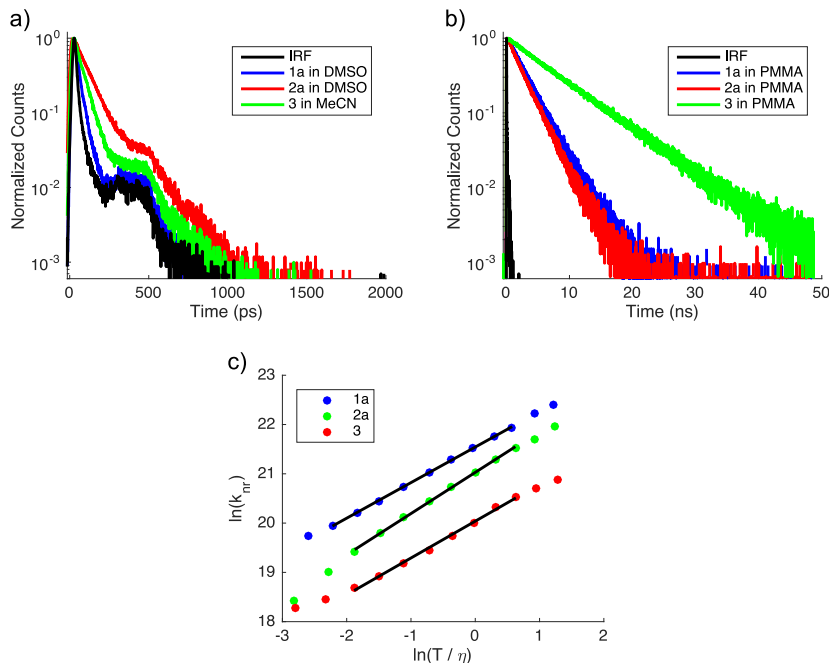


**Figure 7.3:** a) Fluorescence decay curves of **1a**, **2a** and **3** (time-correlated single photon counting, IRF  $\sim 24$  ps) in polar, low-viscosity solvents. b) Fluorescence decay curves of **1a**, **2a** and **3** in PMMA films. c) Nonradiative decay rate of **1a**, **2a** and **3** as a function of viscosity. Viscosity was varied by changing the temperature of glycerol solutions of the probes from 283 K to 328 K.

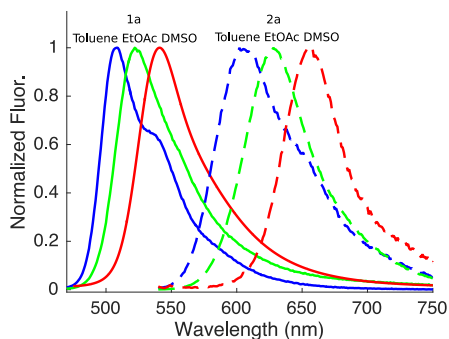
MeCN, but their lifetimes are two orders of magnitude longer in PMMA polymer matrix than in liquid polar solutions (**1a**: 27 ps in DMSO<sup>24</sup>  $\rightarrow$  2.7 ns in PMMA; **2a**: 77 ps in DMSO  $\rightarrow$  2.4 ns in PMMA; **3**: 50 ps in MeCN  $\rightarrow$  7.3 ns in PMMA). These numbers alone suggest **3** as the best viscosity/confinement probe, as its fluorescence increases more than 140 $\times$  in polymer, as compared to the low-viscosity MeCN.

Fluorescence quantum yields of all three compounds exhibit pronounced sensitivity towards the viscosity of their micro-environment. The nonradiative rates of all three compounds can be calculated according to:

$$k_{\text{nr}} = \frac{k_{\text{rad}}}{\Phi_f} - k_{\text{rad}}, \quad (7.1)$$

where  $k_{\text{nr}}$ ,  $\Phi_f$  and  $k_{\text{rad}}$  represent the nonradiative rate constant, fluorescence quantum yield and radiative rate constant, respectively (see ref. 24, Chapter 6, and Appendix 7.4.1). Radiative rate constants were calculated using the fluorescence lifetimes of molecular rotors confined in a polymer matrix, where we assume that PMMA completely confines the rotors and  $k_{\text{nr}} = 0$ . To demonstrate the viscoelastic response of the three molecular rotors, and to compare them quantitatively, we

**Figure 7.4:** Fluorescence emission spectra of **1a** and **2a** in toluene ( $\epsilon = 2.4$ ), EtOAc ( $\epsilon = 6.0$ ) and DMSO ( $\epsilon = 46.8$ ). Relative dielectric permittivities from ref. 5.



measured their fluorescence quantum yields as a function of temperature (from 283 K to 328 K) in glycerol. Viscosity values were interpolated based on the parameters reported in ref. 32. We interpret the obtained nonradiative rates in terms of hydrodynamic theory:

$$k_{\text{nr}}/T = C \eta^{-\alpha}, \quad (7.2)$$

where  $C$  is a (geometry-dependent) constant,  $\alpha$  is a coefficient that describes how the nonradiative decay rate constant correlates with the bulk viscosity, and  $T$  is the temperature (in K). For simplicity, we assume that the intrinsic activation barrier for all three molecules is negligible, and obtain  $\alpha$  values of 0.72 for **1a**, 0.84 for **2a**, and 0.75 for **3**. The observed high correlation values between deactivation rates and bulk viscosities demonstrate that the examined molecules are excellent sensors for bulk viscosity measurements.

The charge transfer character of **1** and **2** renders the spectra of these probes sensitive towards the polarity of their environment. We demonstrate this in Fig. 7.4, where we show fluorescence emission spectra of **1a** and **2a** in non-polar toluene, medium polarity EtOAc, and polar DMSO. We use this behavior to qualitatively estimate the environment polarity of our molecular probes.<sup>33</sup>

## 7.2.2 Photophysical properties of immobilized molecules

Molecules **1**, **2** and **3** have functional groups that allow them to react with terminal amino groups on modified glass surfaces. We immobilize **1** through a well developed peptide coupling procedure (BOP+HOBT+DIPEA), **2** through reaction of the alcohol groups with phosgene to create acyl groups that react with the amino groups on the surface, and **3** through reaction of the amino groups on the surface with the ester group of the BODIPY dye. The resulting cover slips prepared by immobilization of **1**, **2** and **3** are denoted as **CS1**, **CS2** and **CS3**, respectively throughout the rest of this text.

The emission spectra shown in Fig. 7.5 demonstrate that the molecules have been successfully immobilized on the glass surface. Samples functionalized with molecular rotor **2** exhibit excitation and emission spectra that are significantly red-shifted due to extended degree of conjugation compared to **1**, which is beneficial for

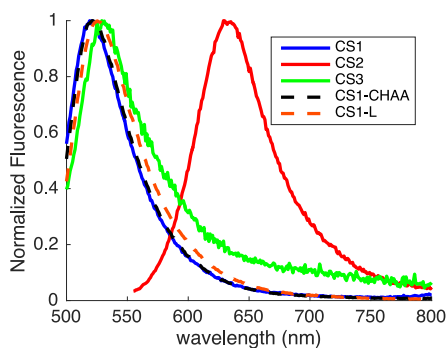


**Figure 7.5:** Normalized emission spectra of dyes immobilized on the glass surface. No solvent was added.  $\lambda_{\text{exc}} = 470$  nm for **CS1**, **CS1-CHAA**, **CS1-L**, and **CS3**;  $\lambda_{\text{exc}} = 530$  nm for **CS2**.

microscopy applications. Since dyes **1** and **2** possess a significant degree of charge-transfer character<sup>20,23,24,34</sup>, they show solvatochromic behavior which provides information about the polarity of their environment. Emission maxima of **CS1** and **CS2** are at 521 and 629 nm for dry cover slips. These are in between the emission maxima of probes **1a** and **2a** in non-polar toluene (509 and 602 nm, respectively) and DMSO (542 and 656 nm). This indicates that the molecules on a surface reside in a moderately polar environment. We examined the potential influence of self-quenching and aggregate formation by functionalizing cover slips with **1** and hydrophobic "spacer" molecules (cyclohexyl acetic acid, CHAA) by reacting amino-functionalized glass, **1** and 10 molar equivalents of CHAA relative to **1**. The resulting samples are labeled **CS1-CHAA** in the text. Attempts to produce more dilute samples by reacting 50 eq. of CHAA relative to **1** resulted in samples unsuitable for contact imaging and characterization (fluorescence was too weak).

The fluorescence spectrum of **CS1-CHAA** is not shifted with respect to that of **CS1** which lacks the spacer molecules, and the spectral width is also identical. This indicates that the presence of aggregates on the surface is unlikely. Interchromophore interactions are therefore not responsible for the observed spectral shift of the surface-bound chromophore relative to **1a** in non-polar toluene. Excited-state stabilization must then originate from interactions with remaining amino-terminated linker molecules on the surface and possibly moisture adsorbed from air. We also attached **1** to glass cover slips functionalized with a longer silane linker (**S2**) that contains two additional secondary amino groups. This type of linker has been proposed to give a more organized surface structure.<sup>35</sup> This sample (**CS1-L**) exhibited a small, but observable spectral shift of  $\sim 5$  nm relative to **CS1/CS1-CHAA** (Fig. 7.5).

We examined the possibility of self-quenching by measuring fluorescence decays of **CS1** and **CS1-CHAA** with time correlated single photon counting. Both samples were prepared in parallel and mounted onto a sample holder of our TC-SPC apparatus (IRF fwhm  $\sim 24$  ps) shortly after drying under an air current to minimize the potential influence of humidity from air, and occasionally moved during the measurement to avoid the influence of photobleaching. Average lifetimes

obtained from triexponential fits of the decay curves (shown in Appendix 7.4.1) measured for dry cover slips were 1.5 ns and 1.7 ns for **CS1** and **CS1-CHAA**, respectively. The relatively long average lifetimes on the dry surfaces indicate a high degree of molecular confinement. The relatively small difference in average lifetime values of the two samples indicates that self-quenching does not have a dramatic influence on excited-state decay. Because we use DMSO in our contact imaging experiments (to reduce background fluorescence and scattering), we measured fluorescence decays of DMSO-wetted **CS1** and **CS1-CHAA** on this setup, as it provides a time resolution that is superior to our FLIM microscope. These attempts, unfortunately, were not successful, because we were not able to collect a sufficient number of photons to fit fluorescence decay curves. Upon wetting the samples in viscous glycerol, the average fluorescence lifetime values decrease to 1.3 ns (**CS1**) and 1.5 ns (**CS1-CHAA**). Attaching **1** to a longer silane (**CS-L**) produced values similar to the ones obtained for **CS1** (1.4 ns for dry and glycerol wetted). Notably, **CS1-L** does not show decrease in  $\tau_{\text{avg}}$  upon wetting with glycerol. We did not find samples labelled **CS1-L** suitable for contact area imaging experiments because addition of DMSO produced micro-droplets over the surface of the sample and within the imaged contact area. This presumably comes as a combined effect of increased hydrophobicity of **CS1-L** relative to **CS1** and low viscosity of DMSO that results in droplet formation within a time-frame that is considerably shorter than needed for us to conduct contact imaging measurements.

### 7.2.3 Contact area measurements

Next, we examine the applicability of molecular rotors for contact area measurements by pressing solid objects on glass surfaces functionalized with molecular rotors **1** (**CS1**), **2** (**CS2**) and **3** (**CS3**). For this purpose, we used a fluorescence confocal microscope with a rheometer mounted on top. A polystyrene (PS) bead was glued to the rheometer tip. In this way we were able to control the position at which the contact occurs, control the contact force, and simultaneously measure the fluorescence response. This experiment is shown in Scheme 7.1.

We first consider samples with surface-bound fluorophores **1** and **2**, **CS1** and **CS2**. Fig. 7.6 shows the PS sphere contacts on these cover slips for various normal forces. The cover slips functionalized with probes **1** and **2** both give excellent contrast between contact and non-contact conditions, indicating that the probes strongly respond to confinement. We compare the experimental images to Hertz theory,<sup>36</sup> which describes the sphere-on-a-flat-surface contact in the absence of roughness. Red circles in Fig. 7.6 represent the apparent contact area calculated according to the Hertz equation (Eq. 7.3), where  $F$  represents the applied load,  $R$  the radius of the PS bead, and  $E^*$  Young's (shear elastic) modulus of the sphere.  $E^*$  is calculated according to Eq. 7.4, where  $E$  and  $\nu$  are the Young's modulus and the Poisson ratio of the sphere material (polystyrene). In the case of a PS sphere pressed on glass, the elastic modulus of the glass can be ignored, since it is more than ten times higher than the PS modulus. The contact area measurements shown in Fig. 7.6 a)-f) are quantitatively compared to the ones

predicted by Hertz theory<sup>36</sup> in Fig. 7.6 g) and h). An atomic force microscopy image of the representative (rough) PS surface is shown in the Appendix (Fig. 7.19). Throughout the examined range, the apparent contact area predicted by Hertz theory agrees well with the overall contact area, but the real contact area is much smaller due to the roughness of the surface.

$$A_{\text{Hertz}} = \pi \left( \frac{3FR}{4E^*} \right)^{2/3} \quad (7.3)$$

$$E^* = \frac{E}{1 - \nu^2} \quad (7.4)$$

Next, we demonstrate the sensitivity of molecular sensors in contact area measurements by comparing the fluorescence technique to an interference based contact area measurement. For this purpose, the reflected light from the contact was collected in addition to the fluorescent light. Destructive interference occurs when the distance between the bead and the surface is  $0.5(m + 0.5)\lambda$ , where  $m$  is an integer ( $m = 1, 2, 3, \dots$ ) and  $\lambda$  is the wavelength of the reflected light. In the centre  $m = 0$ , and destructive interference within the central circle occurs as long as the gap is  $< \lambda/4$  ( $\sim 120$  nm, since  $\lambda = 488$  nm). Molecular rotors, however, become confined only when the axial distance between the surface and the bead is much smaller ( $\sim 9$  nm, see Chapter 8). Because of this, they are able to discriminate the overall contact areas more accurately and resolve fine structure within the contact. An illustrative example is shown in Fig. 7.7, where the contact diameters are illustrated with bars of different color. Differences between contact areas measured by fluorescence and reflection methods can differ when beads of different radii and roughness are used, and the differences between reflection- and fluorescence-based areas are more pronounced under small loads.

To investigate the nature of confinement in contact, we created contacts similar to the ones shown in Fig. 7.6 in a fluorescence lifetime imaging (FLIM) microscope (Fig. 7.8 a)). Two distinct populations (Fig. 7.8 b)) can be observed near the contact zone, due to confined (within contact) and non-confined (out of contact) molecular probes. Pixels that lie outside the contact zone (dark blue regions and representative decay curve in Fig. 7.8 a) and c), respectively) are characterized by average lifetime values around 0.4 ns (lifetime distribution FWHM  $\approx 0.13$  ns, Fig. 7.8 b)). This value is close to the full width at half maximum of our instrument response function, so the actual values may be smaller. Within the contact zone, average lifetime values are narrowly distributed around 1.5 ns (lifetime distribution FWHM  $\approx 0.19$  ns, Fig. 7.8). The histograms of the two populations can not be described by normal distributions, but are skewed towards longer and shorter lifetimes for short- and long-lifetime population, respectively. Fluorescence lifetimes measured within the contact zone are shorter than expected for fully confined molecules ( $\sim 2.7$  ns in PMMA). Decay curves measured with our confocal microscope in different environments are shown in Fig. 7.8 c). The obtained values of  $\tau_{\text{avg}}$  indicate that the average degree of confinement within the contact pixel is comparable to the confinement that molecules experience while immobilized on a

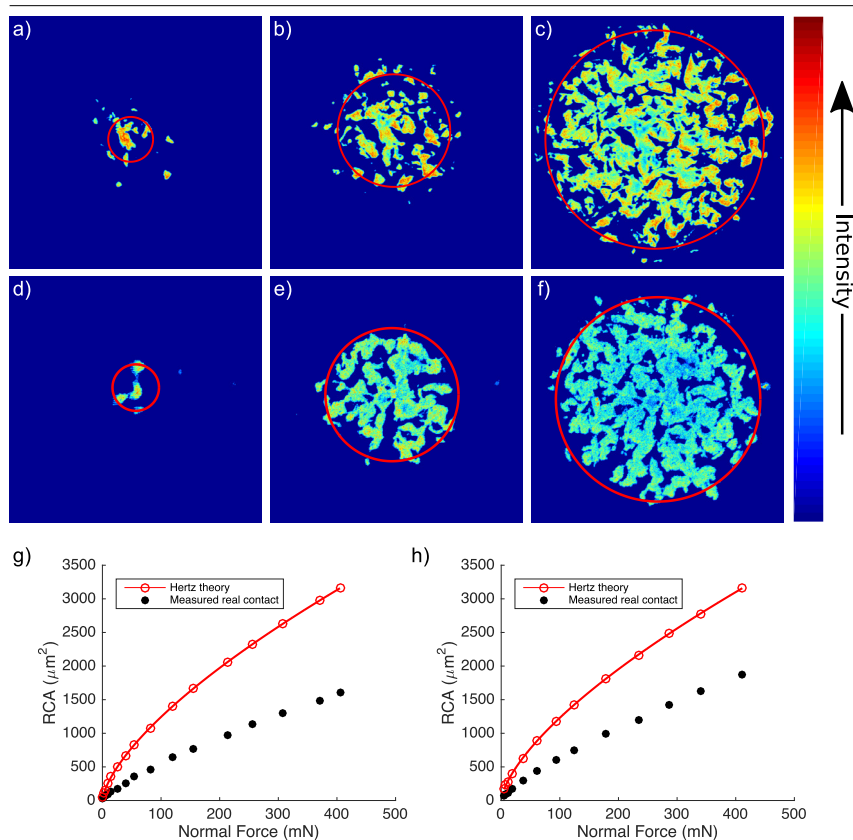


**Figure 7.6:** a), b) and c) fluorescence intensity images of contact between **CS1** and a roughened polystyrene bead, obtained under loads of 1.5, 81.5 and 405.5 mN, respectively. d), e), and f) images obtained with **CS2**, under normal loads of 4.0, 62.0 and 340.0 mN. Red circles indicate the size of the contact area calculated from Eq. 7.3. Image size  $70 \times 70 \mu\text{m}$ . g) and h) show experimentally obtained real contact area (RCA) measured with **CS1** and **CS2**, respectively. Real contact area is directly compared with the apparent contact area predicted by Hertz (red line).<sup>36</sup>

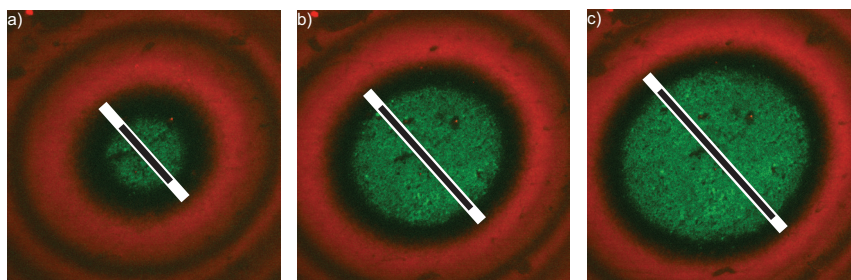


**Figure 7.7:** Comparison of the measured fluorescence response (green) and reflection image (red) obtained by pressing a (relatively smooth) glass bead of 2 mm radius on glass cover slip **CS1**. White bars: contact diameter obtained by reflections; black bars: contact diameter obtained by fluorescence. Applied loads: a) 21 mN; b) 196 mN; c) 410 mN.

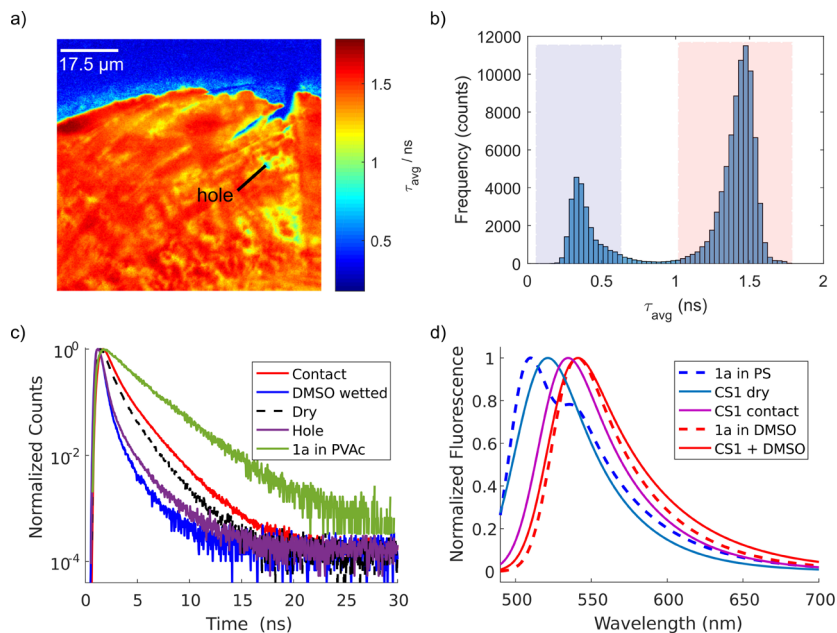


**Figure 7.8:** a) Fluorescence lifetime image of the contact area produced by pressing a smooth polystyrene bead onto DMSO-wetted **CS1** (glass surface functionalized with **1**). Step size  $0.25 \mu\text{m}$ , pixel dwell time 10 ms. Color represents the average arrival time of the photons after the laser pulse at a measured point; b) Histogram of lifetimes from a); c) Representative time correlated single photon counting traces measured with microscope for **1** or **1a** in different environments (integrated over 10-20 points to reduce noise). Holes represent dark areas within the contact zone, as indicated in a); d) Representative fluorescence emission spectra fits of **1** / **1a** in different environments.

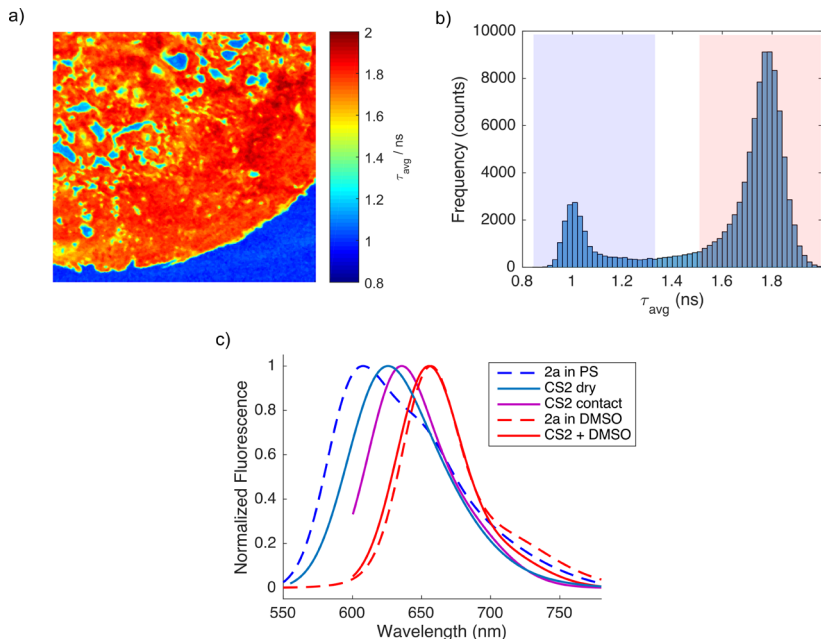


**Figure 7.9:** a) Fluorescence lifetime image of contact area obtained by pressing a PS bead on **CS2** (glass cover slips functionalized with **2**). Image size  $80 \times 80 \mu\text{m}$ , step size 250 nm, dwell time 10 ms; b) Histogram of lifetimes from a); c) Representative fluorescence emission spectra fits of **2** / **2a** in different environments..

dry (1.5 ns) or glycerol wetted (1.3 ns) cover slip. Although the diffraction limit in the lateral plane does not allow us to distinguish possible structural features that are smaller than the optical resolution of our microscope, we can obtain additional information about the molecular environment by measuring fluorescence emission spectra.

Figure 7.8 d) shows examples of fluorescence emission spectra of **1** (or **1a**) measured in different environments. As the polarity of the local environment increases, fluorescence emission spectra shift towards lower energies due to the solvent induced stabilization of the excited state. In low polarity PS matrix the emission maximum is located at 510 nm. Upon immobilization of **1** on glass (**CS1**), the emission maximum shifts to 522 nm. Addition of DMSO on **CS1** results in a pronounced red shift of emission to 541 nm. The emission maximum of **1a** in DMSO is at 542 nm, which indicates that the immobilized probe is fully solvated in the case of DMSO wetted **CS1**. Spectra obtained from the contact zone (upon pressing a PS sphere onto a DMSO wetted **CS1**, see Fig. 7.8 b)) show only a slight hypsochromic shift ( $\sim 5$  nm) relative to the spectrum of **CS1** in DMSO. This indicates that the molecules still reside in a very polar environment within the contact zone and points towards the presence of DMSO.

**CS2** samples show behavior similar to that of **CS1**, but we found that flu-

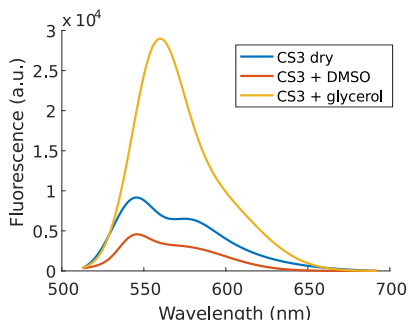


**Figure 7.10:** Fitted fluorescence emission spectra of **CS3** (glass cover slips functionalized with **3**) obtained by soaking the functionalized cover slip with DMSO and glycerol.

orescence lifetimes of surface-bound probe **2** vary with sample preparation procedure (acylation and surface functionalization time). This likely occurs due to self-quenching at high grafting densities,<sup>37</sup> because fluorescence quantum yield of this chromophore is known to be concentration dependent in polymer matrices.<sup>38</sup> Here we report quantities for samples prepared according to the procedure described in the experimental section of this Chapter. A typical fluorescence lifetime image, image histogram, and representative fluorescence emission spectra are shown in Fig. 7.9 a), b) and c), respectively. Fluorescence lifetimes of **CS2** in contact ( $\tau_{\text{avg}} \sim 1.8$  ns) are somewhat longer than those of **CS1**, but they still do not approach the lifetimes measured for the completely confined probe ( $\sim 2.4$  ns). Fluorescence emission spectra shift similarly to those of **CS1**, but spectral shifts seem to be more pronounced due to the higher degree of conjugation which results in a larger excited-state dipole moment.

When similar experiments were performed with **CS3**, the probe did not show any difference in intensities (nor lifetimes) upon confinement with the PS sphere (not shown). Samples did, however, exhibit increased fluorescence intensities when wetted with viscous liquid (glycerol) (Fig. 7.10). This is surprising, because **3** shows sensitivity towards viscosity in solution and when immobilized on the surface just like **1** and **2**.

#### 7.2.4 Discussion

In this work, we demonstrate that fluorescent molecular rotors can be used for very sensitive contact imaging. The fluorescence quantum yields of such probe molecules strongly depend on their ability to undergo large amplitude geometrical distortions that result in fluorescence quenching (and shorter fluorescence lifetimes). When one of the surfaces is functionalized with covalently attached molecular rotors **1** or **2** and brought into contact with another surface, intermolecular motion required for excited-state deactivation is restrained, and the molecules become strongly fluorescent.

The average fluorescence lifetimes for molecular probes **1** - **3** in solution are short, several tens of picoseconds, but they are much longer ( $\sim 1.5$  ns, **CS1**;  $\sim 1.7$  ns, **CS2**) for surface-bound molecular probes **1** and **2**. Apparently, there is a

high degree of molecular confinement due to noncovalent interactions between the probes and the surface. The fluorescence spectral maxima of surface-bound **1** and **2** are in between those in non-polar and polar solvents (Figs. 7.8 d) and 7.9 c)). Wetting of the surface with the polar solvent DMSO, however, largely breaks the molecule-surface interactions, which results in shorter lifetimes ( $\sim 0.4$  ns, **CS1**;  $\sim 1$  ns, **CS2**), and in fluorescence spectra that are the same as in solutions of **1a** and **2a** in the same solvent (Table 7.1).

Upon formation of the contact between the wetted glass surface functionalized with probes **1** or **2** and an object (in our case a polymer or glass bead), intramolecular motion of the probe molecules becomes severely hindered, which results in strong localized fluorescence enhancement that can be imaged with fluorescence microscopy, as demonstrated in Fig. 7.6. Contours of the contact areas extracted from our images are comparable to the ones predicted by the widely accepted Hertz theory,<sup>36</sup> which assumes no roughness and perfect elasticity. Our images, however, enable us to observe the detailed microscopic patterns within the contact zone, allowing us to extract quantitative information about the real microscopic contact. In Chapter 8, we show that the asperities of the sphere in contact are deformed plastically (in contrast with Hertz theory), which gives rise to a nonlinear dependence of the real contact area on load. Since the signal that discriminates contacts from background originates from molecular emitters, our method offers significant improvement in axial contact discrimination over optical measurements based on interference patterns of the reflected light (see Fig. 7.7).

Fluorescence lifetimes that we obtain for surface-bound molecular probe **1** (**CS1**,  $\tau_{\text{avg}} = 1.5$  ns) under contact-induced confinement do not approach the natural radiative lifetime of **1a** ( $3.4 \text{ ns}^{24}$ ) obtained from the Strickler-Berg expression, nor lifetimes that we measure in rigid polymer matrices ( $\tau_{\text{avg}} = 2.7$  ns). Surface-bound **2** behaves similarly. Diluting **1** on the surface with inert cyclohexane acetic acid leads to a small increase of the lifetime to 1.7 ns, indicating that self-quenching due to the high density of fluorophores is not very important. The lifetime of 1.7 ns is still shorter than that of fully confined **1**.

Because **1** is a more robust system in respect to potential self-quenching issues (see Appendix 7.4.3), we use it as a model system to examine the properties of environment within the contact zone. The nonradiative rates for **CS1** within the DMSO-wetted contact (1.5 ns) are uniformly distributed and somewhat smaller than those of the probes in glycerol (1.3 ns), or **CS1** wetted with the same viscous solvent (1.3 ns). We can estimate the "effective viscosity" within the contact zone to be  $\sim 1600$  cP. This may be because of unresolved asperities that are homogeneously distributed throughout the contact between the examined objects. The emission spectra of **CS1** and **CS2** in contact are blue-shifted compared to those in the wetting solvent DMSO. In the contacts, the pressure is quite high (100-250 MPa<sup>39</sup>), and solvent will be squeezed out from the confined space between the cover slip and the contacting surface. This will press the probe molecules towards the surface, and reduce their solvation (Figs. 7.8 d) and 7.9 c)). In addition, the solvation dynamics may be slowed down.

The average fluorescence lifetimes in contact and non-contact points have a

bimodal distribution (Fig. 7.8 b), **CS1**; Fig. 7.9 c), **CS2**). The distribution of lifetimes of **CS1** and **CS2** in contacts tails towards shorter lifetimes. In some pixels, especially at the edge of a contact area, the probes will not be fully confined because the microscopic contact does not cover the whole pixel. This will lead to a larger contribution from the non-confined lifetime of  $\sim 0.4$  ns ( $\sim 1$  ns for **CS2**), and therefore a shorter average lifetime. Apart from this, the bimodal distribution of lifetimes shows a very good contrast, and a sharp turn-on behaviour of fluorescence in contact. The probe molecules in the contacts, seem to experience a homogeneous environment, despite the possible differences in pressure in different parts of the Hertz contact.

A surprising result of the present work is the failure of contact imaging with surface-bound BODIPY derivative **3** (**CS3**), despite the fact that it shows pronounced sensitivity towards confinement in polymers and to viscosity changes (see Fig. 7.3).<sup>40,41</sup> We propose a tentative explanation for this observation, which is based on the different modes of distortion that lead to the nonradiative decay channel. DCDHF-based molecular rotors **1** and **2** are nearly planar in their fluorescent state, and nonradiative decay involves a twisting of the dicyanomethylene unit in non-polar solvents and the phenyl ring in polar solvents. This process requires an increase in volume, which is counteracted by the high pressures in the mechanical contacts. Excited-state decay of **3** on the other hand is accompanied by a decrease of the volume, as the dihedral angle between the phenyl ring and the BODIPY core decreases in going from the locally-excited highly emissive state ( $\sim 50^\circ$ ) towards a conical intersection between the ground- and excited-state potential energy surfaces ( $\sim 20^\circ - 30^\circ$ ), see Chapter 6. Thus, the high pressure in the contact zones may actually compensate for the influence of the increased viscosity in the case of **3**, while the two work together in the case of the DCDHF dyes **1** and **2**.

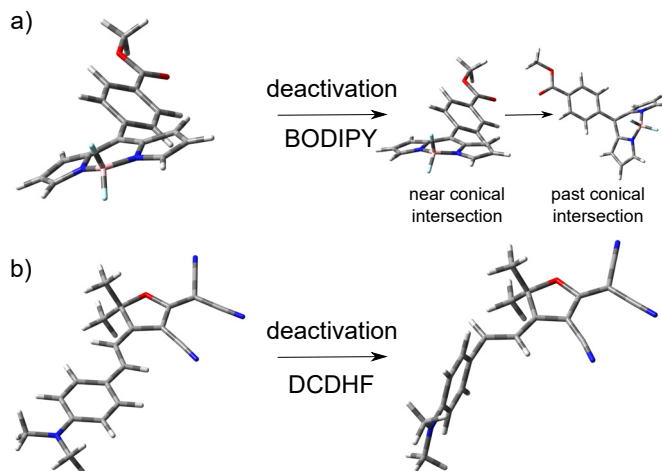


**Figure 7.11:** Excited-state decay pathway schematically shown for: a) **3** (CAM-B3LYP / 6-31+G(d,p)); left structure corresponds to optimized excited-state geometry, right structure corresponds to the molecular geometry near conical intersection; b) **2a** (CAM-B3LYP / 6-31+G(d)); optimized excited-state geometry is shown on the left, dark TICT state on the right.

## 7.3 Conclusion

In this work we compare three fluorescent molecular rotors in solution and provide photophysical characterization of these molecules while immobilized on a surface with the goal of imaging the microscopic real contact area between solid objects. DCDHF molecular rotors provide excellent response towards confinement and molecular scale contact detection sensitivity in the axial direction. Because of this, our contact imaging method provides significant improvement in axial contact discrimination over measurement that are based on interference patterns of the reflected light. Two distinct populations of surface-bound probes can be observed in proximity of the contact zone. The population with shorter average fluorescence lifetime is associated with unconfined and fully solvated molecular probes on the surface, while the population associated with longer average fluorescence lifetime is associated with probes that are partially confined by the rigid environment within the contact. This is further indicated by the fact that the probes are partially solvated due to the limited amount of available space within contact, which is not sufficient for them to form a complete solvation shell. The BODIPY based molecular rotor **3**, however, did not show measurable response upon surface-induced confinement. While DCDHF derivatives twist away from planarity along the excited-state decay reaction coordinate, BODIPY-based rotor **3** becomes increasingly planar and requires less space to perform this motion. The high pressure in the contact areas will relatively favor process with a negative activation volume, which counteracts the viscosity effect for **3**.

## 7.4 Appendix to Chapter 7

### 7.4.1 Photophysical behavior of **2** and **2a**

In our previous work<sup>24</sup> we have shown that excited-state deactivation of **1** takes place through two pathways. The pathway that is favored in non-polar solvents mainly involves torsional motion around dicyanomethylene double bond, which results in conical intersection between the ground- and excited-state potential energy surfaces and involves no transient intermediates. The pathway favored in polar solvents involves a twist around the single bond connecting the phenyl and furan rings, and results in formation of the dark twisted intramolecular charge-transfer state intermediate. Our experimental and theoretical data shown below suggest that excited-state deactivation of extended derivatives **2** and **2a** is similar to that of **1**. Twisting motion around  $\beta_1$  does not result in a different conformer, but twisting around  $\beta_2$  does. We have optimized these conformers at the CAM-B3LYP/6-31+G(d) level of theory. The two conformers have different relative energies ( $\sim 0.16$  kcal mol<sup>-1</sup>) and slightly different excitation energies (3.04 and 2.98 eV for higher and lower energy conformer, respectively). Ground state rotation around the  $\beta_2$  bond is expected to result in structural inhomogeneity of the ground state molecular geometries, and upon photoexcitation, to result in an excited-state conformer distribution. Ground state dipole moments calculated for both conformers are very similar (18.27 and 18.06 D), and variations in solvent polarity are thus not expected to have a significant influence on relative populations between the two.

Optimization of the first excited state (TD CAM-B3LYP/6-31+G(d)) produces geometries that are similar to those of the ground-state. These structures are shown in Fig. 7.13, and are referred to as ES1 (higher-energy conformer,  $\mu = 20.34$  D) and ES2 (lower-energy conformer,  $\mu = 20.57$  D). Both geometries are emissive (2.73 eV for ES1 with oscillator strength of 1.57; 2.66 eV for ES2 with oscillator strength of 1.38). Unconstrained optimization of the geometry in which  $\beta_1$  is initially set to 90° results in twisted, highly polar and dark (osc. strength = 0) local minimum that we refer to as  $ES_{\beta_1}$  ( $\mu = 35.88$  D), with excited- to ground-state energy gap of 2.42 eV. Partial optimization of the geometry in which  $\beta_2$  is fixed to 90° produces a highly polar structure  $ES_{\beta_2}$  ( $\mu = 30.84$  D) with excited- to ground-state energy gap of 2.33 eV (osc. strength 0.12), but the subsequent optimization without imposed constraints converges back to the ES2 structure, which is a global minimum.

The molecular dipole moment calculated for the optimized  $\gamma$ -twisted excited-state  $\gamma$ -twisted geometry (Fig. 7.12,  $\mu = 11.17$  D) indicates that twisting around the dicyanomethylene double bond is less likely to take place in polar environment, as the large drop in molecular dipole moment is expected to make this twist unfavorable in polar solvents. In analogy to **1a**, twisting around this bond is expected to result in a conical intersection and momentary ground state repopulation.<sup>24</sup>

We note that the calculations we present here are preliminary results that we obtain in vacuum. In analogy to previous results reported for **1**, introducing solvent

**Table 7.2:** Molecular properties obtained for excited-state geometries (isolated molecules, CAM-B3LYP / 6-31+G(d)). See Figure 7.13 for relevant geometries mentioned in this table.

Variable	ES <sub>1</sub>	ES <sub>2</sub>	ES <sub>β<sub>1</sub></sub>	ES <sub>β<sub>2</sub></sub> (β <sub>2</sub> fixed to 90°)	ES <sub>γ</sub>
E(GS) <sup>(a)</sup>	3.74	3.77	16.89	24.13	40.17
E(S <sub>1</sub> ) <sup>(b)</sup>	66.44	64.95	72.57	77.68	49.84
f <sup>(c)</sup>	1.57	1.38	0.00	0.12	0.00
μ <sup>(d)</sup>	20.34	20.57	35.88	30.84	11.17

<sup>a</sup> Energies of excited-state geometries (kcal mol<sup>-1</sup>) relative to the ground-state minimum energy; <sup>b</sup> First excited-state energies (kcal mol<sup>-1</sup>) relative to the ground-state minimum energy; <sup>c</sup> Oscillator strength values; <sup>d</sup> Excited-state molecular dipole moment. Geometries labelled ES<sub>β<sub>1</sub></sub> and ES<sub>γ</sub> are fully optimized twisted geometries (dihedrals β<sub>1</sub> and γ ~90°, while ES<sub>β<sub>2</sub></sub> is partially optimized geometry in which β<sub>2</sub> dihedral value was fixed to 90°.

through PCM (or some other formalism), can be expected to dramatically lower the energy of the highly polar twisted intermediates ES<sub>β<sub>1</sub></sub> and ES<sub>β<sub>2</sub></sub> relative to the global minimum that we obtain in vacuum. Our current results are summarized in Table 7.2 and relevant structures are shown in Figure 7.13.

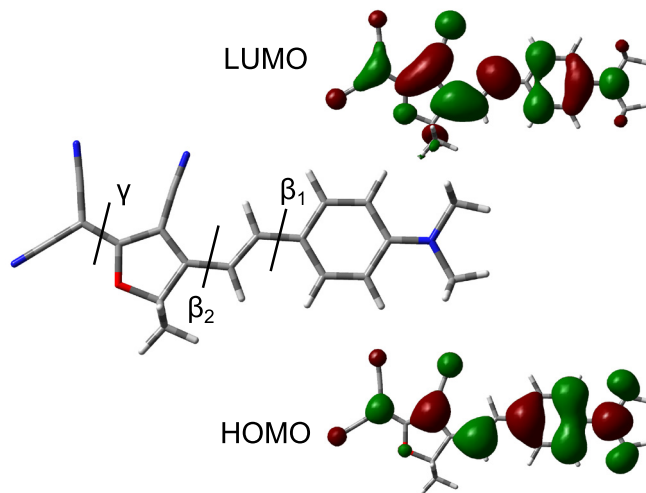


**Figure 7.12:** Optimized ground-state geometry (CAM-B3LYP/6-31+G(d)) of molecular rotor **2a** with indicated relevant torsional motions.

We measured vis-pump vis-probe transients of compound **2a** in EtOAc, MeOH and DMSO. In case of all three solvents, stimulated emission (SE) time traces could be well fitted with triexponential functions. A typical single time trace with the fit is shown in Fig. 7.14. While the two shorter components are associated with the increase of the SE, the longest component is associated with the decrease of SE. The first component is very short (hundreds of fs) and likely occurs due to vibra-

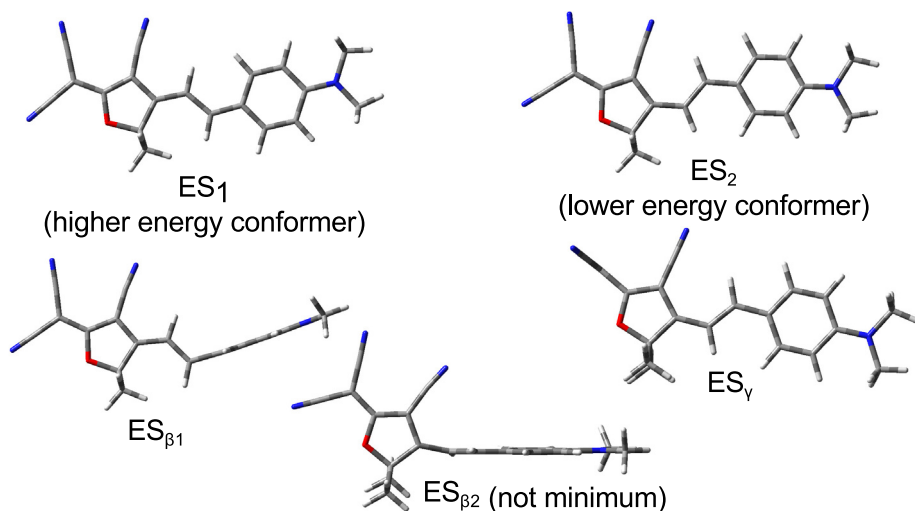


**Figure 7.13:** Relevant excited-state structures obtained by TD CAM-B3LYP/6-31+G(d) level of theory.

tional relaxation and solvation. The second short component (few ps) can be due to solvation. The third (and slowest) component is attributed to the excited-state population decay. The decay time of this component is in good agreement with the time constant obtained by measuring fluorescence decays using time correlated single photon counting. Decay-associated difference spectra produced by means of global analysis of the transient-data matrices measured in EtOAc, MeOH and DMSO are shown in Fig. 7.15 a), c) and e), while evolution-associated difference spectra (sequential model) are shown in Fig. 7.15 b), d) and f). Although theoretical results indicate that excited-state deactivation of **2a** takes place through  $\gamma$ -twist in vacuum, excited-state depopulation via  $\beta_1$ -twisted intramolecular charge transfer intermediate is likely to occur in the polar solvents used in our experimental study. As  $\beta_1$  twist results in large decoupling of the donor and acceptor parts of the molecule, it produces a large dipole moment which is expected to be significantly stabilized by a polar environment. From Onsager solvation theory<sup>42</sup>, calculated energies and dipole moments for the ES2 and ES $_{\beta_1}$  (Table 7.2) and estimated cavity radius of 5.77 Å we estimate that the ES $_{\beta_1}$  will be approximately 17 kcal mol<sup>-1</sup> lower in energy relative to ES2 in EtOAc ( $\epsilon = 6^5$ ). Our transient absorption experiments, however, were not able to capture formation of transient intermediates that could be associated with the TICT state formation in a straight-forward manner. A potential cause for this is that ES $_{\beta_1} \rightarrow$ GS internal conversion is an order of magnitude (or more) faster than the conversion of ES2 to ES $_{\beta_1}$ . From data presented in Table 7.2, calculated ground-state dipole moment of 18.3 D for ES $_{\beta_1}$  and Onsager theory<sup>42</sup>, we estimate that the excited- to ground-

**Table 7.3:** Time constants ( $\tau_x$ ) obtained by global analysis of transient-data matrices and fluorescence quantum yields ( $\Phi_f$ ) of **2a**. Fluorescence decay rates obtained by time correlated single photon counting technique are given in brackets.

Solvent	$\tau_1$ / ps	$\tau_2$ / ps	$\tau_3$ / ps	$\Phi_f$ / %
EtOAc	0.6	6.7	245.1 (254)	4.5
MeOH	0.5	5.5	30.3 (28)	0.6
DMSO	0.4	2.3	77.0 (78)	1.4

state energy gap of the  $\beta_1$ -twisted geometries is  $\sim 15$ -36 kcal mol $^{-1}$  (depending on the solvent). Such a small difference in energy would, judging by the experimental data for  $S_1 \rightarrow S_0$  internal conversion reported in ref. 43 for highly conjugated polyenes, result in  $S_1 \rightarrow S_0$  internal conversion rates of a few ps. Such an efficient internal conversion would result in a very low population of the  $ES_{\beta_1}$  state that can not be detected by our transient measurements.

Excited-state deactivation through  $\gamma$  bond twist is expected to result in a conical intersection with the ground state potential energy surface similar to the case of **1a**.<sup>24</sup> This excited-state decay pathway is likely a dominant excited-state deactivation pathway of **2a** in non-polar solvents, due to a low dipole moment that is associated with the  $\gamma$ -twisted geometry ( $ES_\gamma$ ).<sup>24</sup>

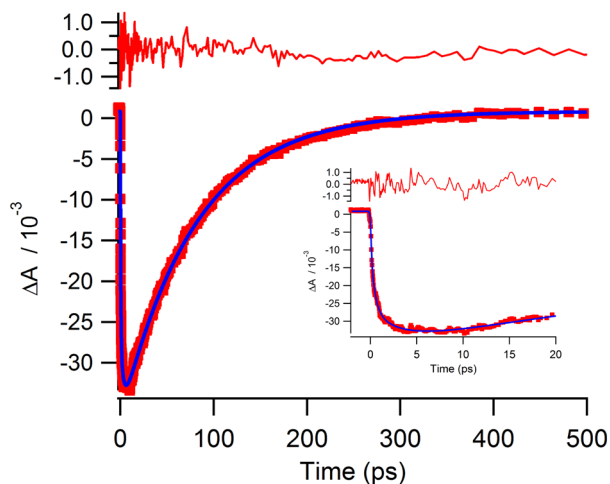


**Figure 7.14:** Stimulated emission time trace of **2a** in DMSO ( $\lambda_{exp} = 488$  nm;  $\lambda_{mon} = 585$  nm). Triexponential fit yields time constants of  $\tau_1 = 0.5$ ,  $\tau_2 = 3.0$  and  $\tau_3 = 80.3$  ps.

Time constants obtained by global analysis of transient-data matrices and fluorescence quantum yields ( $\Phi_f$ ) are summarized in Table 7.3.

In order to gain more insight into excited-state deactivation pathways of **2a**, we measured its fluorescence intensities as a function of the Onsager polarity func-

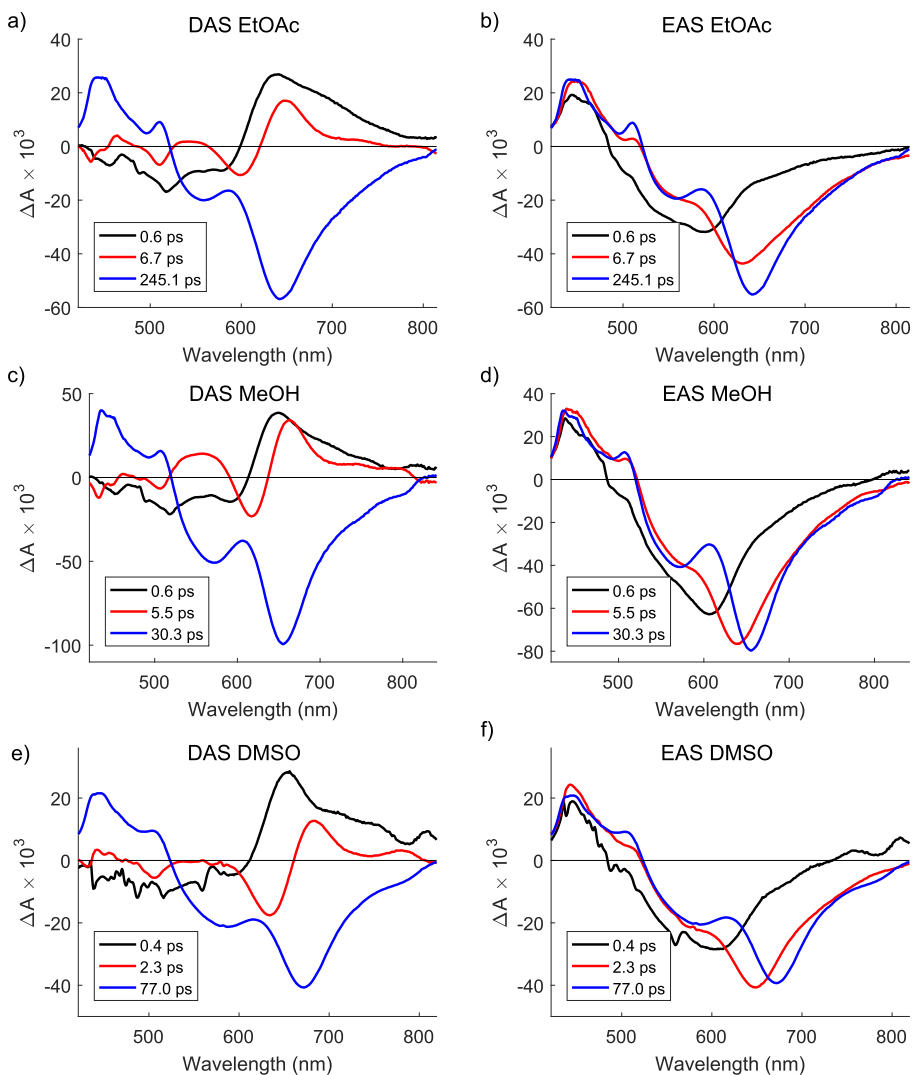


**Figure 7.15:** Decay associated and evolution associated difference spectra of **2a** in EtOAc, MeOH and DMSO.

tion  $f(\epsilon) = (\epsilon - 1)/(2\epsilon + 1)^{33}$  in toluene/MeCN mixtures by titrating toluene solutions of **2a** ( $\Phi_{f,\text{tol}} = 1.1\%$ ) with MeCN ( $\Phi_{f,\text{MeCN}} = 1.6\%$ ). Relative permittivities  $\epsilon$  of these mixtures were obtained by interpolation of the experimental data reported in reference 44. Upon addition of MeCN to toluene solutions of **2a**, fluorescence intensities (corrected for absorption differences) initially increase and reach a maximum ( $\sim 18 \times$  relative to the intensity measured in pure toluene). After this point, fluorescence intensities decrease towards pure MeCN

solution. Absorbance-corrected emission spectra and integrated fluorescence intensities from this experiment are shown in Figure 7.16. Such behavior is consistent with the presence of two excited-state deactivation pathways with opposite polarity response, as indicated by DFT calculations described above, and similar to the trends observed for **1a**.<sup>24</sup>

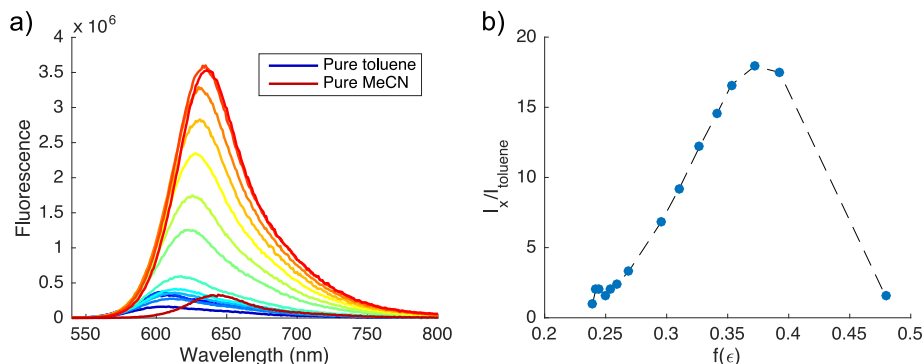


**Figure 7.16:** a) Fluorescence spectra and b) normalized integrated fluorescence intensities obtained for **2a** in toluene/MeCN mixtures.

### 7.4.2 Fluorescence decays of surface-bound probe **1**

To examine the influence of different immobilization procedures and fluorophore concentrations on the surface on fluorescence lifetimes of surface-bound **1**, we measured fluorescence decays of such samples (FWHM  $\sim 24$  ps). In cases where we measured the influence of glycerol, we applied a drop of glycerol on our samples functionalized with **1** and sandwiched them between two clean cover slips. Fluorescence decay curves mentioned in the main text are shown in Fig. 7.17.

### 7.4.3 Self-quenching of probe **2** on the surface

Willetts *et al.* reported that chromophore **2** undergoes concentration-dependent self-quenching in polymer matrices.<sup>38</sup> In our experiments, we observe a similar phenomenon which seems to be dependent on grafting density of **2** on the surface. This effect is illustrated in Fig. 7.18, where we show fluorescence decays measured for dry **CS2** measured on confocal microscope. In these samples, **2** was allowed to react with amino-functionalized cover slips for 30 mins. and 24 hours, while other parameters were kept identical (including the reaction flask). The sample that was prepared by reacting probe **2** with amino-functionalized cover slips for 24 hrs. shows significantly shorter fluorescence decay compared to the sample that was allowed to react only for 30 mins. A similar effect in polymer matrices was not observed for chromophore **1**.<sup>38</sup>

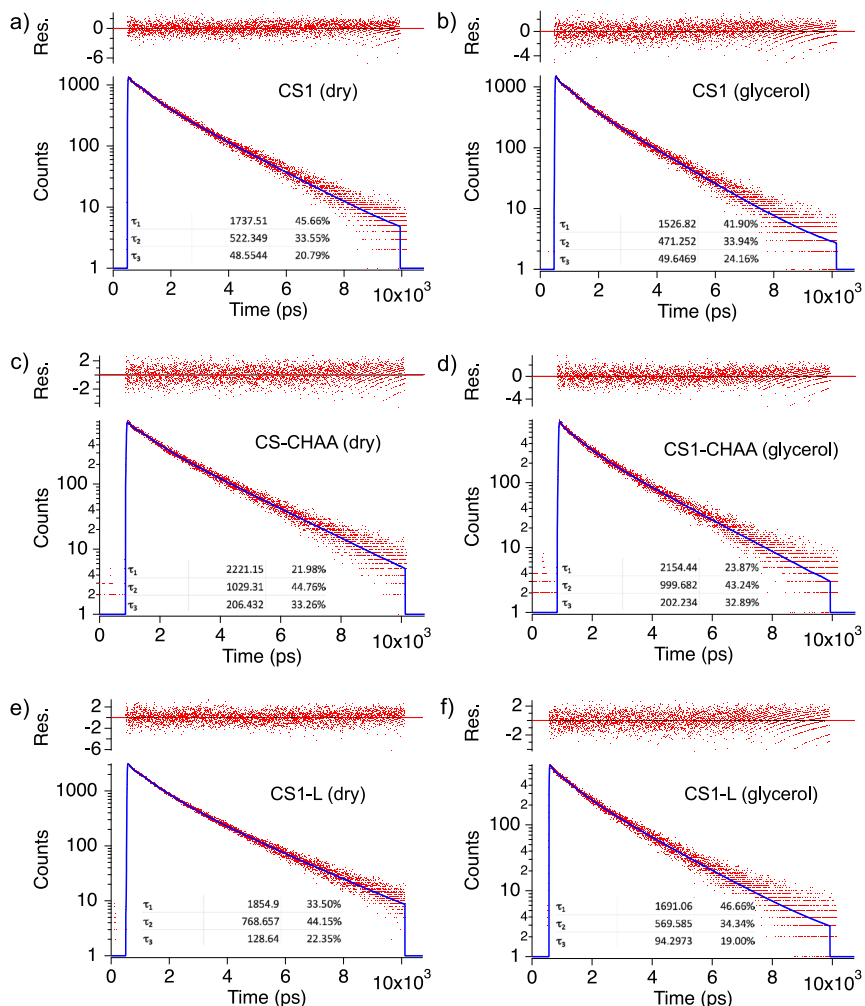


**Figure 7.17:** Fluorescence decay curves of surface-bound chromophore **1** immobilized through different procedures. Red dots are measured curves, and blue lines are triexponential fits.

#### 7.4.4 AFM measurements of PS bead

The examined cover slips with immobilized molecular rotors are very smooth (within the spatial resolution of our AFM). A typical AFM image of clean glass cover slip is shown in Fig. 7.19 a). Periodic "waviness" of the surface of the clean glass cover slips occurs because of the manufacturing process of glass cover slips (float glass). Occasional bumps can be observed, likely due to the presence of dust particles. AFM images of the beads used in our measurements, however, show roughness on the  $\mu\text{m}$  scale. A typical example is shown in Figure 7.19 b). The

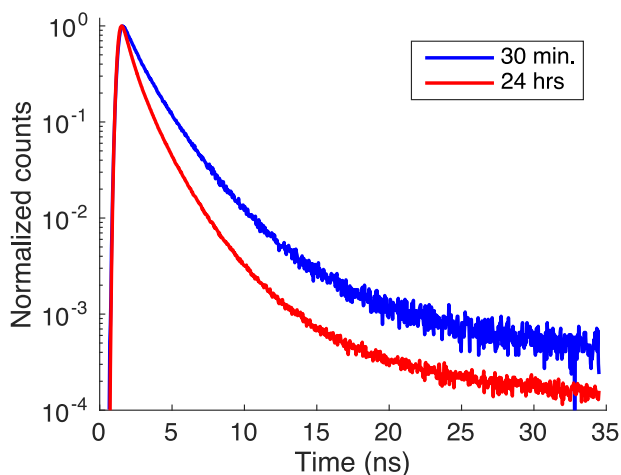


**Figure 7.18:** Influence of reaction time on fluorescence decays of **CS2** samples.

roughness of clean cover slips is on nm scale (standard deviation in Fig. 7.19 a) is 1.2 nm), while the roughness of PS beads used in our experiments is on  $\mu\text{m}$  scale (standard deviation in Fig. 7.19 b) is 220 nm).

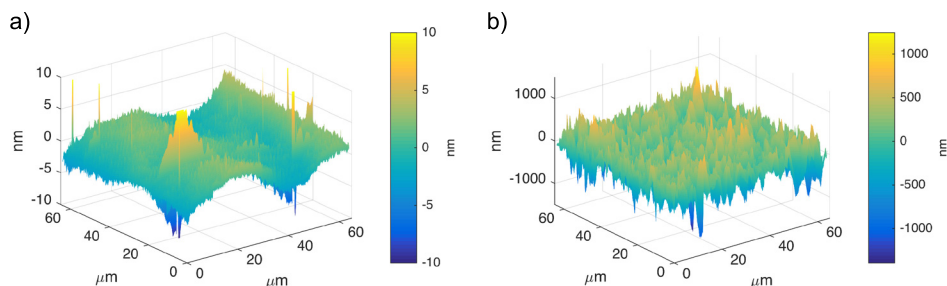


**Figure 7.19:** AFM measurement of a) a typical clean glass cover slip; b) a typical PS bead used in contact area imaging experiments. Curvature of the PS bead was subtracted using a polynomial fit.

### 7.4.5 Surface density of molecular rotors

Molecular rotors are immobilized on the surface by reacting amino-functionalized glass cover slips with chromophores that contain reactive functional groups. Surface reactions and layer formation of APTES (and similar silanes) is relatively complex, and detailed discussion about the nature of mono-(or multi) layer silane structures or potential defects on the surface falls out of the scope of this text.

In order to roughly estimate the grafting density of chromophores on our functionalized surface, we have measured absorption spectra relative to the silanized

cover slips. A typical absorption measurement is shown in Figure 7.20. Absorbance is very low, as expected from a single dye layer attached to the surface. Compared to solutions, absorption spectra of **CS1** and **CS2** appear to be broader. The band shape of **1** and **2** on the surface suggests the presence of additional bands at high energies. Since locations and shapes of high energy bands look different in the case of **CS1** and red shifted **CS2**, photoexcitation to higher excited states provides possible explanation for these bands, although the reason for this transition being more pronounced on a surface is not known to us. Nevertheless, peak absorption values enable us to roughly estimate the grafting density on the surface. If we assume that the optical cross sections of immobilized molecules are the same as in toluene solutions ( $62\,200\text{ M}^{-1}\text{cm}^{-1}$  and  $42\,300\text{ M}^{-1}\text{cm}^{-1}$  for **1a** and **2a**, respectively), Lambert-Beer law can be used to estimate the number of molecules per unit area to be  $\sim \frac{A}{2\epsilon}$  (since both sides of cover slips are functionalized). The grafting density obtained in this way is  $\sim 1$  molecules per  $10\text{ nm}^2$  for both **CS1** and **CS2**. Such a low grafting density should, in principle, not allow for a large degree of homo FRET and self quenching.<sup>33</sup>

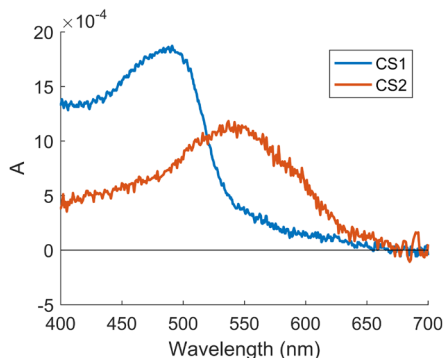


**Figure 7.20:** Absorption spectra of cover slips used in contact imaging.

### 7.4.6 Additional examples of surface contacts

Surface contacts can be imaged by pressing different materials onto the functionalized cover slips, as demonstrated in Figure 7.21 that shows additional contact imaging examples obtained by pressing spheres of different materials and roughness on **CS1**.

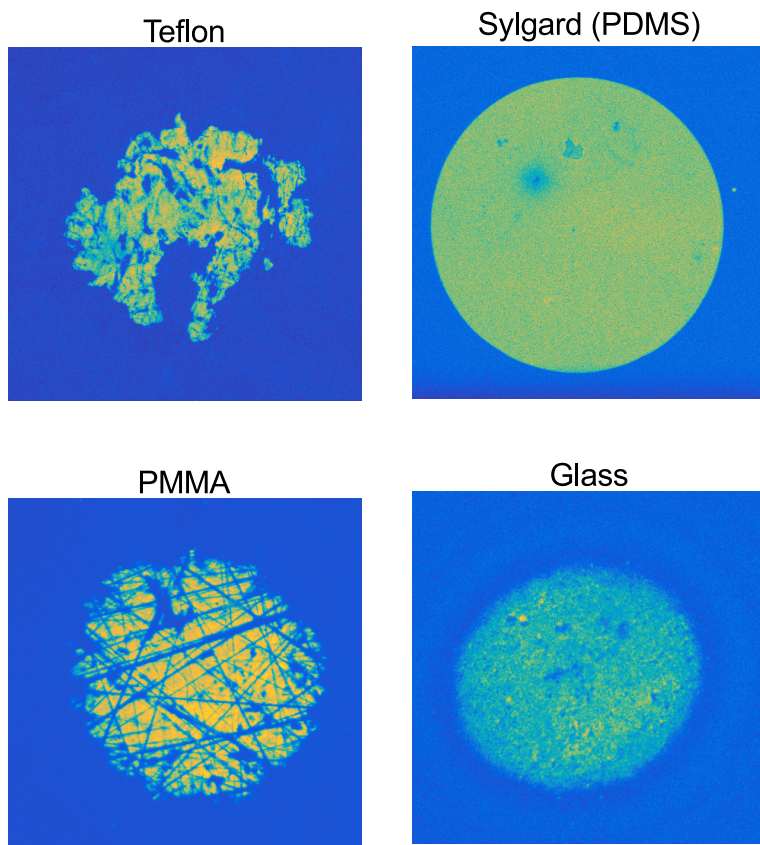


**Figure 7.21:** Contacts imaged with different surfaces pressed on **CS1**. Image sizes were  $330 \times 330 \mu\text{m}$ ,  $360 \times 360 \mu\text{m}$ ,  $140 \times 140 \mu\text{m}$  and  $90 \times 90 \mu\text{m}$  for teflon, sylgard (polydimethylsiloxane), PMMA and glass, respectively. Contacts shown here are illustrative examples that demonstrate the applicability of our method for a range of bead materials and are not quantitatively discussed in the text.

## References

1. Suhina, T.; Weber, B.; Carpentier, C. E.; Lorincz, K.; Schall, P.; Bonn, D.; Brouwer, A. M. *Angew. Chem. Int. Ed.* **2015**, *54*, 3688–3691.
2. Szeri, A. Z. *Tribology: friction, lubrication, and wear*; McGraw-Hill, 1980.
3. Amontons, G. *De la resistance causée dans les machines*; Mem. l'Académie R. A, 1699.
4. Persson, B. *Sliding friction: physical principles and applications*; Springer Science & Business Media, 2013.
5. Haynes, W. M. *CRC handbook of chemistry and physics*; CRC press, 2014.
6. Gao, J.; Luedtke, W.; Gourdon, D.; Ruths, M.; Israelachvili, J.; Landman, U. *J. Phys. Chem. B* **2004**, *108*, 3410–3425.
7. Carbone, G.; Bottiglione, F. *J. Mech. Phys. Solids* **2008**, *56*, 2555–2572.
8. Bowden, F.; Tabor, D. *Proc. R. Soc. A* **1939**, 391–413.
9. Greenwood, J.; Williamson, J. *Proc. R. Soc. A* **1966**, 300–319.
10. Greenwood, J.; Tripp, J. *Proc. Inst. Mech. Eng.* **1970**, *185*, 625–633.
11. Whitehouse, D. J.; Archard, J. *Proc. R. Soc. A* **1970**, *316*, 97–121.
12. Bush, A.; Gibson, R.; Thomas, T. *Wear* **1975**, *35*, 87–111.
13. Persson, B. N. *J. Chem. Phys.* **2001**, *115*, 3840–3861.
14. Holm, R. *Electric contacts: theory and application*; Springer Science & Business Media, 1967.
15. Dyson, J.; Hirst, W. *Proc. Phys. Soc. London, Sec. B* **1954**, *67*, 309.
16. Dieterich, J. H.; Kilgore, B. D. *Pure Appl. Geophys.* **1994**, *143*, 283–302.
17. Rubinstein, S. M.; Cohen, G.; Fineberg, J. *Nature* **2004**, *430*, 1005–1009.
18. Rubinstein, S. M.; Shay, M.; Cohen, G.; Fineberg, J. *Int. J. Fract.* **2006**, *140*, 201–212.
19. Svetlizky, I.; Fineberg, J. *Nature* **2014**, *509*, 205–208.
20. Lord, S. J.; Lu, Z.; Wang, H.; Willets, K. A.; Schuck, P. J.; Lee, H.-l. D.; Nishimura, S. Y.; Twieg, R. J.; Moerner, W. *J. Phys. Chem. A* **2007**, *111*, 8934–8941.
21. Wang, H.; Lu, Z.; Lord, S. J.; Moerner, W.; Twieg, R. J. *Tetrahedron Lett.* **2007**, *48*, 3471–3474.
22. Han, L.; Jiang, Y.; Li, W.; Li, Y.; Liao, J. *Mater. Lett.* **2008**, *62*, 1495–1498.
23. Willets, K. A.; Callis, P. R.; Moerner, W. *J. Phys. Chem. B* **2004**, *108*, 10465–10473.
24. Suhina, T.; Amirjalayer, S.; Mennucci, B.; Woutersen, S.; Hilbers, M.; Bonn, D.; Brouwer, A. M. *J. Phys. Chem. Lett.* **2016**, *7*, 4285–4290.
25. Gubler, U.; He, M.; Wright, D.; Roh, Y.; Twieg, R.; Moerner, W. *Adv. Mater.* **2002**, *14*, 313–317.
26. Melanson, J. A.; Smithen, D. A.; Cameron, T. S.; Thompson, A. *Can. J. Chem.* **2013**, *92*, 688–694.

27. Tang, X.; Pan, L.; Jia, K.; Tang, X. *Chem. Phys. Lett.* **2016**, *648*, 114–118.
28. Perez-Moreno, J.; Zhao, Y.; Clays, K.; Kuzyk, M. G.; Shen, Y.; Qiu, L.; Hao, J.; Guo, K. *J. Am. Chem. Soc.* **2009**, *131*, 5084–5093.
29. Kalambet, Y.; Kozmin, Y.; Mikhailova, K.; Nagaev, I.; Tikhonov, P. *J. Chemometrics* **2011**, *25*, 352–356.
30. Würth, C.; Grabolle, M.; Pauli, J.; Spieles, M.; Resch-Genger, U. *Nat. Protoc.* **2013**, *8*, 1535–1550.
31. Frisch, M. J. et al. Gaussian 09 Revision D.01. Gaussian Inc. Wallingford CT 2009.
32. Cheng, N.-S. *Ind. Eng. Chem. Res.* **2008**, *47*, 3285–3288.
33. Lakowicz, J. R. *Principles of Fluorescence Spectroscopy*; Springer Science & Business Media, 2006.
34. Willets, K. A.; Nishimura, S. Y.; Schuck, P. J.; Twieg, R. J.; Moerner, W. *Acc. Chem. Res.* **2005**, *38*, 549–556.
35. King, M. D.; Kihara, M. T.; Lott, G. A.; Hill, M. W.; Scatena, L. F. *J. Phys. Chem. C* **2014**, *118*, 15804–15815.
36. Hertz, H. *J. Reine Angew. Math.* **1881**, *92*, 156–171.
37. Conley, N. R.; Pomerantz, A. K.; Wang, H.; Twieg, R. J.; Moerner, W. *J. Phys. Chem. B* **2007**, *111*, 7929–7931.
38. Willets, K. A.; Ostroverkhova, O.; He, M.; Twieg, R. J.; Moerner, W. *J. Am. Chem. Soc.* **2003**, *125*, 1174–1175.
39. Weber, B.; Suhina, T.; Junge, T.; Pastewka, L.; Brouwer, A. M.; Bonn, D. *Submitted*
40. Alamiry, M. A.; Benniston, A. C.; Copley, G.; Elliott, K. J.; Harriman, A.; Stewart, B.; Zhi, Y.-G. *Chem. Mater.* **2008**, *20*, 4024–4032.
41. Levitt, J. A.; Chung, P.-H.; Kuimova, M. K.; Yahiolu, G.; Wang, Y.; Qu, J.; Suhling, K. *ChemPhysChem* **2011**, *12*, 662–672.
42. Suppan, P. *J. Photochem. Photobiol. A* **1990**, *50*, 293–330.
43. Frank, H. A.; Desamero, R. Z.; Chynwat, V.; Gebhard, R.; Van Der Hoef, I.; Jansen, F. J.; Lugtenburg, J.; Gosztola, D.; Wasielewski, M. R. *J. Phys. Chem. A* **1997**, *101*, 149–157.
44. Ritzoulis, G.; Papadopoulos, N.; Jannakoudakis, D. *J. Chem. Eng. Data* **1986**, *31*, 146–148.